


APOGEE-2S Mg–Al anti-correlation of the metal-poor globular cluster NGC 2298

Ian Baeza¹, José G. Fernández-Trincado² , Sandro Villanova¹, Doug Geisler^{1,3,4}, Dante Minniti^{5,6}, Elisa R. Garro⁵, Beatriz Barbuy⁷, Timothy C. Beers⁸, and Richard R. Lane⁹

¹ Departamento de Astronomía, Universidad de Concepción, Casilla 160-C, Concepción, Chile
e-mail: ibaeza2017@udec.cl, svillanova@astro-udec.cl

² Instituto de Astronomía, Universidad Católica del Norte, Av. Angamos 0610, Antofagasta, Chile
e-mail: jose.fernandez@ucn.cl

³ Departamento de Astronomía, Universidad de La Serena, 1700000 La Serena, Chile

⁴ Instituto de Investigación Multidisciplinario en Ciencia y Tecnología, Universidad de La Serena, Benavente 980, La Serena, Chile
⁵ Depto. de Cs. Físicas, Facultad de Ciencias Exactas, Universidad Andrés Bello, Av. Fernández Concha 700, Las Condes, Santiago, Chile

⁶ Vatican Observatory, 00120 Vatican City State, Italy

⁷ Universidade de São Paulo, IAG, Rua do Matão 1226, Cidade Universitária, São Paulo 05508-900, Brazil

⁸ Department of Physics and JINA Center for the Evolution of the Elements, University of Notre Dame, Notre Dame, IN 46556, USA

⁹ Centro de Investigación en Astronomía, Universidad Bernardo O'Higgins, Avenida Viel 1497, Santiago, Chile

Received 4 March 2022 / Accepted 14 April 2022

ABSTRACT

We present detailed elemental abundances and radial velocities of stars in the metal-poor globular cluster (GC) NGC 2298, based on near-infrared high-resolution ($R \sim 22\,500$) spectra of 12 members obtained during the second phase of the Apache Point Observatory Galactic Evolution Experiment (APOGEE-2) at Las Campanas Observatory as part of the seventeenth Data Release (DR 17) of the Sloan Digital Sky Survey IV (SDSS-IV). We employed the Brussels Automatic Code for Characterizing High accuracy Spectra (BACCHUS) software to investigate abundances for a variety of species including α elements (Mg, Si, and Ca), the odd- Z element Al, and iron-peak elements (Fe and Ni) located in the innermost regions of NGC 2298. We find a mean and median metallicity $[\text{Fe}/\text{H}] = -1.76$ and -1.75 , respectively, with a star-to-star spread of 0.14 dex, which is compatible with the internal measurement errors. Thus, we find no evidence for an intrinsic $[\text{Fe}/\text{H}]$ abundance spread in NGC 2298. The typical α -element enrichment in NGC 2298 is overabundant relative to the Sun, and it follows the trend of other metal-poor GCs. We confirm the existence of an Al-enhanced population in this cluster, which is clearly anti-correlated with Mg, indicating the prevalence of the multiple-population phenomenon in NGC 2298.

Key words. stars: abundances – stars: chemically peculiar – globular clusters: individual: NGC 2298 – techniques: spectroscopic

1. Introduction

Globular clusters (GCs) are important long-lived time capsules that provide information about the primordial evolutionary stages of their host galaxies. For several decades, GC stars have been known to display a zoo of peculiarities, such as light-element (Carretta et al. 2009b; Pancino et al. 2017; Schiavon et al. 2017; Masseron et al. 2019; Mészáros et al. 2020, 2021; Geisler et al. 2021, and references therein) and heavy-element (Carretta & Bragaglia 2021; Marino et al. 2021; Fernández-Trincado et al. 2022, 2021a) abundance variations over a wide range of metallicities, which have been attributed to the multiple-populations (MPs) phenomenon (for a thorough review, see Bastian & Lardo 2018).

The southern cluster NGC 2298, located in the constellation Puppis, has long been recognized to be among the most metal-poor GCs in the Milky Way (MW; Hesser & Shawl 1985; McWilliam et al. 1992). However, the metallicity estimates reported for this object have covered a range from $[\text{Fe}/\text{H}] = -1.96$ to -1.71 (see e.g., Frogel et al. 1983; Cohen 1983; Zinn

& West 1984; Zinn 1985; McWilliam et al. 1992; Geisler et al. 1995; Salaris & Cassisi 1996; Carretta & Gratton 1997; Kraft & Ivans 2003; Pritzl et al. 2005; Carretta et al. 2009a; Carrera et al. 2013; Roediger et al. 2014; Yong et al. 2014), creating some uncertainty regarding its status as one of the most metal-poor systems. This cluster is also well known for its lack of a clear indication of MPs along the main sequence (MS; Piotto et al. 2015), as well as likely along the horizontal branch (HB) population (Rani et al. 2021), in near-UV/optical color-magnitude diagrams (CMDs). However, its red-giant branch (RGB) displays clear evidence for both first- and second-generation stars (e.g., Milone et al. 2017).

NGC 2298 is a particularly interesting GC, as its origin and nature still remains controversial. For instance, some studies have proposed that it is likely associated with the Monoceros progenitor galaxy (Crane et al. 2003; Martin et al. 2004; Forbes & Bridges 2010); however, more recent studies conducted by Massari et al. (2019) and Malhan et al. (2022) have linked this GC to the Gaia-Sausage/Enceladus merger (Belokurov et al. 2018; Helmi et al. 2018). A few previous and more recent studies

have also suggested the presence of extra-tidal features around NGC 2298 (Leon et al. 2000; Balbinot et al. 2011; Carballo-Bello et al. 2018; Piatti & Carballo-Bello 2020; Sollima 2020; Ibata et al. 2021); however, their existence has been questioned based on more recent investigations of deep imaging from the Dark Energy Camera (Zhang et al. 2022).

While NGC 2298 has been widely studied photometrically (in the optical and UV), detailed spectroscopic information about it remains sparse. Furthermore, spectroscopic evidence for the existence of multiple stellar populations in this GC has not been reported in the literature yet. Located at 15.1 kpc (Baumgardt & Vasiliev 2021) from the Galactic center, it is an old (~ 12 – 13 Gyr; Monty et al. 2018) GC that lies in a region of relatively low foreground interstellar reddening, with $E(B-V) \sim 0.14$ – 0.16 (Kraft & Ivans 2003; Piotto et al. 2015; Monty et al. 2018), making it an excellent candidate for the study of MPs in GCs at a low Galactic latitude ($b \sim -16^\circ$). In the present work, we report the first high-resolution near-infrared (NIR) spectral study of elemental-abundance estimates for a variety of chemical species for a sample of 12 sources in the innermost regions of NGC 2298 and we characterize its chemical composition. For the first time, we report information on the main element families, namely the α elements (Mg, Si, Ca), the odd- Z element Al, and the Fe-peak elements (Fe and Ni).

The structure of this paper is as follows. Section 2 describes the data, and Sect. 3 describes the identified cluster members. Sections 4 and 5 describe the derivation of atmospheric parameters and elemental abundances for the individual stars. Section 6 presents our abundance analysis, and Sect. 7 provides our concluding remarks.

2. Data

The Apache Point Observatory Galactic Evolution Experiment II survey (APOGEE-2; Majewski et al. 2017) is one of the internal programs of the Sloan Digital Sky Survey-IV (SDSS-IV; Blanton et al. 2017). It was developed to provide precise radial velocities (RV errors $< 1 \text{ km s}^{-1}$) and detailed chemical abundances for an unprecedented large sample of giant stars, aiming to unveil the dynamical structure and chemical history across the entire MW. The APOGEE-2 instruments (capable of observing up to 300 objects simultaneously) are high-resolution ($R \sim 22\,500$), NIR spectrographs (Wilson et al. 2019) observing all the components of the MW (halo, disk, and bulge) from the Northern Hemisphere on the 2.5 m telescope at the Apache Point Observatory (APO, APOGEE-2N; Gunn et al. 2006) and the Southern Hemisphere on the Irénée du Pont 2.5 m telescope at the Las Campanas Observatory (LCO, APOGEE-2S; Bowen & Vaughan 1973). Each instrument records most of the H band ($1.51 \mu\text{m}$ – $1.69 \mu\text{m}$) on three detectors, with coverage gaps between ~ 1.58 – $1.59 \mu\text{m}$ and ~ 1.64 – $1.65 \mu\text{m}$, and with each fiber subtending a $\sim 2''$ diameter on-sky field of view in the northern instrument and $1.3''$ one in the southern instrument.

DR 17 (Abdurro'uf et al. 2022) is the final release of the APOGEE-2 survey from SDSS-IV. It includes all APOGEE-2 data taken at APO through November 2020 and at LCO through January 2021. The dual APOGEE-2 instruments have observed more than 700 000 stars throughout the MW. We refer the reader to Zasowski et al. (2017), Beaton et al. (2021), and Santana et al. (2021) for further details regarding the targeting strategy of the APOGEE-2 survey.

Spectra for this project were reduced as described in Nidever et al. (2015); they were also analyzed using the

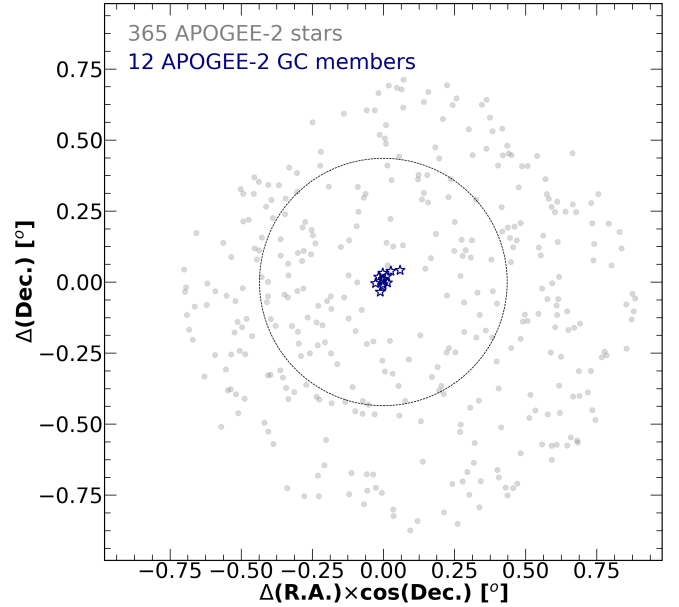


Fig. 1. Spatial distribution of sources (gray dots) surveyed by APOGEE-2S toward the NGC 2298 field. Potential cluster members analyzed in this work are marked with empty, navy blue “star” symbols. The large black dashed circle highlights the cluster tidal radius, $r_t = 26.12$ arcmin at $d_\odot = 9.83 \pm 0.17$ kpc (Baumgardt & Vasiliev 2021). The image is oriented with the east pointing to the right and north pointing up.

APOGEE Stellar Parameters and Chemical Abundance Pipeline (ASPCAP; García Pérez et al. 2016), and the libraries of synthetic spectra described in Zamora et al. (2015). The accuracy and precision of the atmospheric parameters and chemical abundances are extensively analyzed in Holtzman et al. (2018) and Jönsson et al. (2018, 2020), while details regarding the custom H -band line list are fully described in Shetrone et al. (2015), Hasselquist et al. (2016), Cunha et al. (2017), and Smith et al. (2021).

3. Sample

The metal-poor GC NGC 2298 was included in the targeting strategy of the APOGEE-2S program at the end of the survey. Here we analyze for the first time the APOGEE-2S spectra for potential members of NGC 2298 – centered on $\alpha = 06:48:59.41$ and $\delta = -36:00:19.1$ – observed from LCO by the APOGEE-2S survey in January 2021.

The APOGEE-2S plug-plates (PlateID = 12836 and 12837), containing the NGC 2298 field (LocID = 7253), are centered on $(\alpha, \delta) \sim (102.35549^\circ, -36.0852^\circ)$ and contain 365 science fibers. From these, 12 stars lie very close to the cluster center, which is well within the tidal radius ($r_t \lesssim 26.12$ arcmin)¹ at $d_\odot = 9.83 \pm 0.17$ kpc (Baumgardt & Vasiliev 2021), as shown in Fig. 1.

Figure 2 shows that the 12 sources analyzed in this work share common properties making them very likely NGC 2298 members, that is to say their position along the main branches of the cluster CMD in the $Gaia$ EDR3 bands; nominal $Gaia$ EDR3 proper motions, $(\mu_\alpha \cos \delta; \mu_\delta) = (3.320 \pm 0.025; -2.175 \pm 0.026) \text{ mas yr}^{-1}$; radial velocity, $RV = 147.15 \pm 0.57 \text{ km s}^{-1}$ (Vasiliev & Baumgardt 2021); and metallicity. The same figure (left and middle panel) also shows the membership probability

¹ <https://people.smp.uq.edu.au/HolgerBaumgardt/globular/parameter.html>

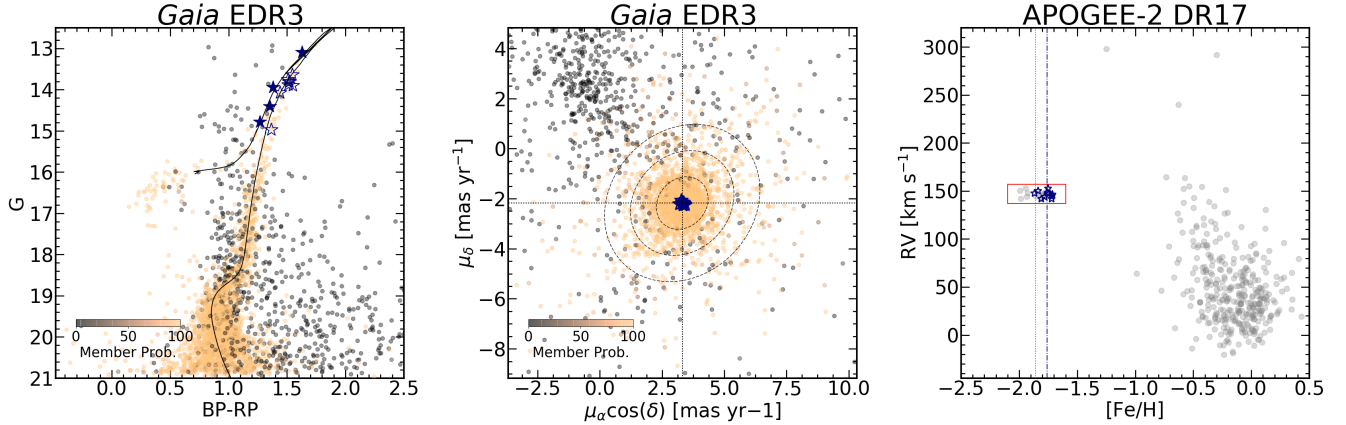


Fig. 2. Main physical properties of NGC 2298 stars. *Left panel:* *Gaia* optical CMD with membership probabilities color-coded as shown in the inset. RGB and AGB stars are denoted by open and filled symbols, respectively. A PARSEC isochrone of 12 Gyr and a metallicity of -1.75 is also overplotted with black solid lines. *Middle panel:* *Gaia* EDR3 vector point diagram (VPD). The three concentric dashed ellipses represent the 1-, 2-, and 3- σ level of the highest likelihood cluster members with $>90\%$ membership probability. The two black dashed lines are shown for visual aids and show the nominal proper motions of the cluster taken from Vasiliev & Baumgardt (2021). *Right panel:* metallicity ($[\text{Fe}/\text{H}]$) versus radial velocity for 365 APOGEE-2S stars toward the NGC 2298 field. ASPCAP results are denoted by gray dots, while the BACCHUS results are denoted by navy blue star symbols for the 12 cluster members. The red box, which is arbitrarily limited between $[\text{Fe}/\text{H}] = -2.1$ and -1.6 , centered on $\text{RV} = 147.15 \text{ km s}^{-1}$ according to Baumgardt & Vasiliev (2021), and limited between $\pm 10 \text{ km s}^{-1}$, encloses the highest likelihood cluster members with ASPCAP (gray dots) and BACCHUS (navy blue stars) determinations. The gray dotted and navy blue dash-dotted lines mark the average $\langle [\text{Fe}/\text{H}] \rangle$ of the 12 NGC 2298 stars analyzed in this work, and they are centered at $\langle [\text{Fe}/\text{H}] \rangle = -1.86$ (ASPCAP results) and $\langle [\text{Fe}/\text{H}] \rangle = -1.76$ (BACCHUS results), respectively. The 12 stars examined in this work are denoted by navy blue star symbols in all panels.

provided by Vasiliev & Baumgardt (2021) for the NGC 2298 field. The 12 target stars occupy the region of the CMD dominated by highest likelihood cluster stars on the red giant branch (RGB) and asymptotic giant branch (AGB).

The APOGEE-2S spectra used in this work have a typical signal-to-noise ratio (S/N) larger than 109 pixel^{-1} , which was reached from two (ten stars) and four (two stars) field visits, making these spectra ideal to obtain reliable elemental abundances for several chemical species accessible from the H band in the metal-poor regime. Additionally, we find the typical radial velocity scatter (VSCATTER) to be less than 0.3 km s^{-1} for all sources in our sample, with no strong evidence for radial velocity variations that might affect the resulting elemental abundances.

Figure 2 also shows the radial velocity against the metallicity for the 365 sources surveyed by APOGEE-2S in the region of this GC. ASPCAP- $[\text{Fe}/\text{H}]$ determinations are highlighted by gray open symbols, while the BACCHUS- $[\text{Fe}/\text{H}]$ ones (see Sect. 5) are marked with navy blue symbols. This figure reveals that BACCHUS- $[\text{Fe}/\text{H}]$ is systematically offset by roughly 0.1 dex to higher metallicity compared to the ASPCAP- $[\text{Fe}/\text{H}]$ abundance ratio, which is most likely due to systematics between BACCHUS and ASPCAP, similar to other studies of the APOGEE-2 spectra (see, e.g., Masseron et al. 2019; Fernández-Trincado et al. 2020; Mészáros et al. 2020).

4. Atmospheric parameters

Adopting the typical value $R_V = 3.1$, $E(B - V) = 0.14$ (Monty et al. 2018) and a distance of 9.83 kpc (Baumgardt & Vasiliev 2021), we first de-reddened the optical *Gaia* EDR3 photometric bands. We obtain T_{eff} and $\log(g)$ from photometry by determining the reddening-corrected CMD of NGC 2298. We then horizontally projected the position of each observed star until it intersected the PARSEC (Bressan et al. 2012) isochrone, chosen to have an age of ~ 12 Gyr (Monty et al. 2018), a metallicity of $[\text{Fe}/\text{H}] \sim -1.75$ (see Table A.1), and an assumed T_{eff} and $\log(g)$ to be the temperature and gravity at the point of the isochrones

that has the same optical magnitude as the star. Since no differential reddening was present, we could easily separate RGB from AGB stars. For each group, we used the corresponding part of the isochrone to obtain the parameters, that is, we used the isochrone RGB to obtain T_{eff} and $\log(g)$ for RGB stars, and the isochrone AGB to obtain T_{eff} and $\log(g)$ for AGB stars. Finally, microturbulence velocities ξ_t were determined empirically with the BACCHUS code (Masseron et al. 2016). The resulting atmospheric parameters and elemental abundances for the 12 stars examined in the innermost regions of NGC 2298 are listed in Table A.1.

5. Abundance determinations

Once the final atmospheric parameters were computed, abundances for a variety of elements could be derived line-by-line using the BACCHUS code. Thus, chemical abundances were derived for six atomic species (Mg I, Al I, Si I, Ca I, Fe I, and Ni I) from a local thermodynamics equilibrium (LTE) analysis using BACCHUS combined with the MARCS model atmospheres (Gustafsson et al. 2008), and following the same technique as described in several APOGEE-2 works (see, e.g., Fernández-Trincado et al. 2021b, 2019, for instance), and summarized here for guidance. With the atmospheric parameters determined in Sect. 4, the first step consisted of determining the metallicity from selected Fe I lines, the micro-turbulence velocity (ξ_t), and the convolution parameter. Other chemical species not reported in this work were found to have very weak lines and/or were too heavily blended by telluric features to provide reliable abundances.

With the metallicity and main atmospheric parameters fixed, we then computed the abundance of each chemical species as follows: (a) we performed a synthesis using the full set of atomic and molecule line lists fully described in Smith et al. (2021). This set of lines is internally labeled as *turbospec.20180901t20.atoms* and *turbospec.20180901t20.molec* based on the date of creation in the format YYYYMMDD. This

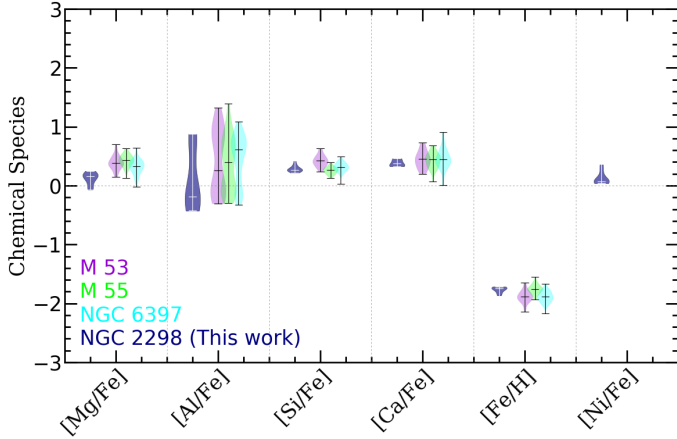


Fig. 3. $[X/Fe]$ and $[Fe/H]$ abundance kernel density estimation comparison between NGC 2298 (navy blue symbols on the *left*) and cluster stars (violet, lime green, and cyan symbols for M 53, M 55, and NGC 6397, respectively, on the *right*) taken from Mészáros et al. (2020). Each violin-type shape indicates the median and limits of the distribution with horizontal lines.

was used to find the local continuum level via a linear fit. (b) We then performed cosmic ray and telluric line rejections, before (c) estimating the local S/N. (d) We automatically selected a series of flux points contributing to a given absorption line, and then (e) we derived abundances by comparing the observed spectrum with a set of convolved synthetic spectra characterized by different abundances. Subsequently, four different abundance determination methods were used: (1) line-profile fitting; (2) core line-intensity comparison; (3) global goodness-of-fit estimate; and (4) an equivalent-width comparison. Each diagnostic yields validation flags. Based on these flags, a decision tree then rejects or accepts each estimate, keeping the best-fit abundance. We adopted the ξ^2 diagnostic for the abundance choice because of its robustness. However, we stored the information from the other diagnostics, including the standard deviation between all four methods.

6. Elemental abundances

The present study substantially contributes to the chemical characterisation of the metal-poor GC NGC 2298. Our sample of 12 cluster members allows us to investigate any intra-cluster abundance variations. Figure 3 summarizes the resulting elemental abundances for six chemical species, including α elements (Mg, Si, and Ca), the odd-Z element Al, and iron-peak elements (Fe and Ni) that were investigated from APOGEE-2S spectra for the 12 stars in the innermost region of NGC 2298. Table A.1 contains the abundance values for $[Mg/Fe]$, $[Al/Fe]$, $[Si/Fe]$, $[Ca/Fe]$, $[Fe/H]$, and $[Ni/Fe]$ derived by the BACCHUS code scaled to the Solar reference value from Asplund et al. (2005).

We remark that no conclusive answers can be drawn for C, N, and O from $^{12}C^{14}N$, ^{16}OH , and $^{12}C^{16}O$, as these lines become too weak to be detected or accurately measured at the metallicity and temperature range of our NGC 2298 stars. For this reason, we choose not to speculate on the interpretation of C, N, and O abundances for the present sample.

Overall, the results for NGC 2298 are in reasonable agreement with other GCs of a similar metallicity for almost all species. However, NGC 2298 exhibits median values for $[N/Fe]$ and $[Mg/Fe]$ which are slightly lower than M 53, M 55, and

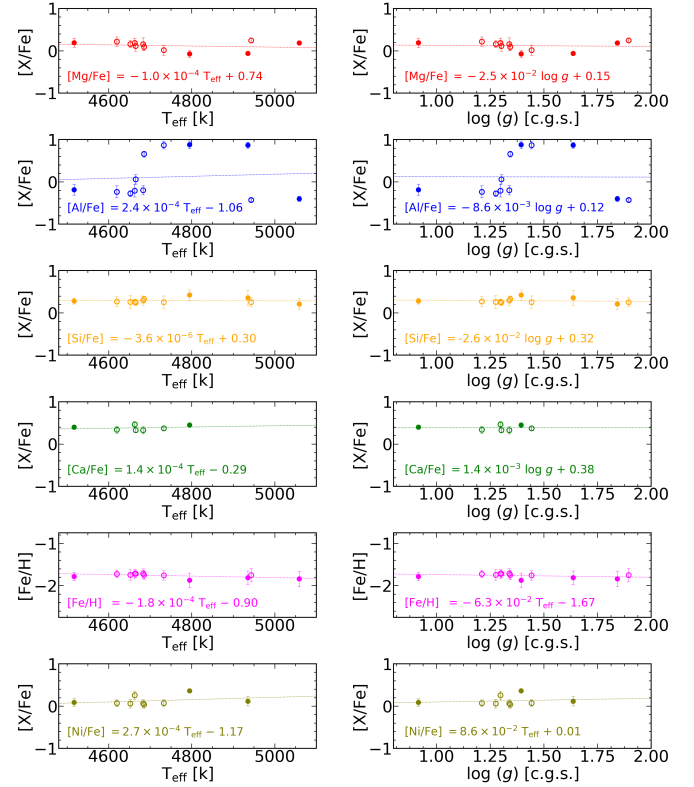


Fig. 4. Elemental abundances and uncertainties of α elements (Mg, Si, and Ca), the odd-Z element Al, and Fe-peak elements (Fe and Ni) determined with BACCHUS for stars in NGC 2298, as a function of the atmospheric parameters (T_{eff} and $\log g$). The RGB and AGB stars are denoted by open and filled symbols, respectively. The dashed lines and inset notation represent the linear regression of the data.

NGC 6397 (Mészáros et al. 2020), suggesting a likely different chemical-enrichment history and/or distinct birth conditions.

Figure 4 demonstrates a lack of abundance dependence on the effective temperature or surface gravity, as well as on the evolutionary status (RGB or AGB) for Mg, Al, Si, Ca, Fe, or Ni at the metallicity of NGC 2298.

In the following, we describe the chemical-enrichment level of NGC 2298 for the different chemical species examined in this work.

6.1. α elements (Mg, Si, and Ca)

From inspection of Table A.1, the median and mean values for the α elements from Mg to Ca in NGC 2298 are overabundant ($\gtrsim +0.12$) compared to the Sun, supporting the idea that the main contributors to the chemistry of this cluster have likely been mostly provided by supernovae (SNe) II events (Tsujimoto & Bekki 2012), which have been formed before SNe Ia could significantly contribute with iron. This is a feature very common to almost all Galactic GCs with a similar metallicity in the outer halo, and a metallicity below $[Fe/H] = -1.0$.

The NGC 2298 sample has a star-to-star spread in $[Si/Fe] \sim 0.15$ dex and $[Ca/Fe] \sim 0.13$ dex, which is slightly larger than the measurement uncertainties for each species, with the exception of $[Mg/Fe]$. There is a significant $[Mg/Fe]$ spread of ~ 0.3 dex, exceeding the observational uncertainties, which is anti-correlated with $[Al/Fe]$ (see Sect. 6.2). However, the $[Mg/Fe]$ abundance ratio by itself exhibits a median value that

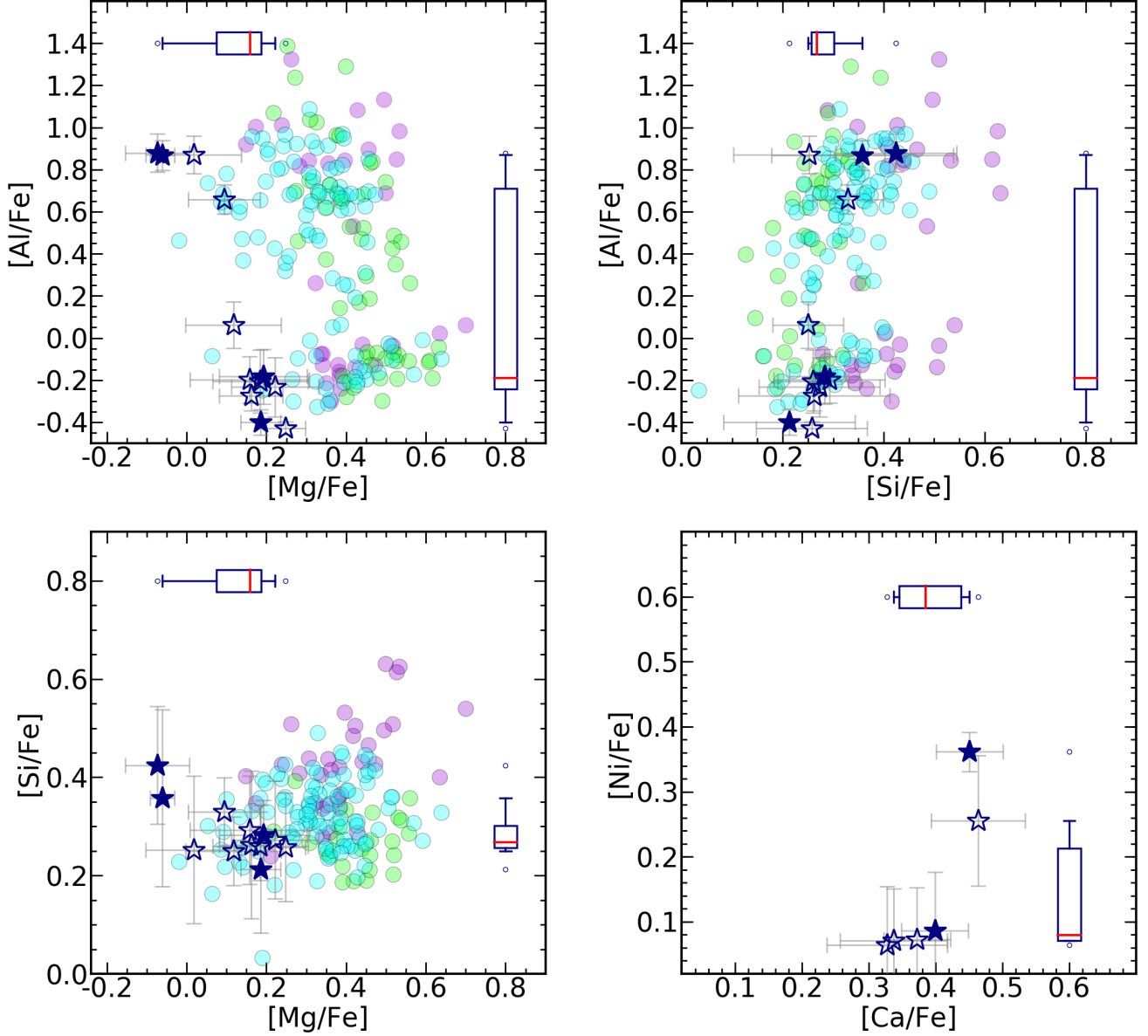


Fig. 5. Combined elemental abundances of α elements (Mg, Si, and Ca), the odd-Z element Al, and iron-peak elements (Fe and Ni) compared to cluster stars taken from Mészáros et al. (2020) at a similar metallicity as NGC 2298. Stars in NGC 2298 are denoted by navy blue star symbols, with open and filled symbols indicating RGB and AGB stars, respectively. The inset box plots indicate, with horizontal red lines, the median as well as the 5th and 95th percentile limits of the distribution of each chemical species in NGC 2298. The gray symbols represent the internal uncertainties of each element.

is systematically offset by roughly 0.2 dex lower than M 53, M 55, and NGC 6397 stars from Mészáros et al. (2020), as can be appreciated in Fig. 3. There are several reasons for a systematic offset between our $[\text{Mg}/\text{Fe}]$ determinations and those determined by Mészáros et al. (2020). For instance, non-local thermodynamic equilibrium (NLTE) and/or 3D effects are currently not modeled when fitting the APOGEE spectra; and/or the systematic differences in the temperature scales.

Figure 5 reveals an apparent Mg–Si anti-correlation. The existence of a Mg–Si anti-correlation in NGC 2298 implies the presence of leakage from the MgAl chain into Si production through the $^{26}\text{Al}(p, \gamma)^{27}\text{Si}(e^-, \nu)^{27}\text{Al}(p, \gamma)^{28}\text{Si}$ reactions at a high temperature. In the absence of this leakage, we would expect a simple correlation between Mg and Si since they are both α elements (see, e.g., Yong et al. 2005; Carretta et al. 2009b; Mészáros et al. 2020). We find that some of the stars

in NGC 2298 exhibit a higher Si abundance than their Mg-rich counterparts, confirming the likely occurrence of hot proton burning in the early populations of NGC 2298. It is important to note that the evidence for this Mg–Si anti-correlation does not exist for the other GCs at a similar metallicity as that of NGC 2298.

An Al–Si correlation is also observed in NGC 2298, as can be appreciated in Fig. 5. Yong et al. (2005), Carretta et al. (2009b), Mészáros et al. (2015), Masseron et al. (2019), and Mészáros et al. (2020) interpreted the Al–Si correlation as a signature of ^{28}Si leakage from the Mg–Al chain. Interestingly, most of the Si-enriched stars in NGC 2298 also seem to correspond to the Mg-depleted and Al-enhanced cluster population, which are likely the result of Ne–Na and Mg–Al cycles occurring in the H-burning shell of the first-generation stars whose nucleosynthetic products were later distributed through the cluster. We stress that,

regarding any possible analysis bias, we have not been able to find any dependence of the abundances with the evolutionary status.

6.2. The odd-Z element Al

Similar to the result reported 30 years ago by McWilliam et al. (1992), we confirm that this cluster also hosts a clear population of Al-enhanced stars with $[Al/Fe] \gtrsim +0.5$, which is significantly higher than typical Galactic abundances of $[Al/Fe] < +0.5$ (for the typical first-generation stars). Figure 5 also clearly reveals two distinct groups in the Mg–Al plane; one of them lies in the region dominated by the lowest $[Al/Fe]$ abundances with slightly super-Solar $[Mg/Fe]$ abundance ratios rather than sub-Solar ones (often called first-generation stars or unenriched stars), while the second group is governed by higher $[Al/Fe]$ abundances with the lowest $[Mg/Fe]$ abundances, containing a fraction of stars well below $[Mg/Fe] \approx 0$ (called second-generation or enriched stars). We conclude that the intra-GC abundance variations reported in Fig. 5 are indicative of the presence of the MP phenomenon in NGC 2298, but the origin of the polluting material remains elusive based on these data.

We also detect a significant star-to-star spread ($\gtrsim 1.29$ dex) in $[Al/Fe]$, as can be appreciated in Fig. 5. An anti-correlation between Al and Mg is clearly present in NGC 2298, showing the signs of proton burning of the envelope material by the Mg–Al cycle, which is commonly present in most metal-poor GCs. It is clear that the extended distribution of Al and Mg is much larger than the typical errors of $[Al/Fe]$ and $[Mg/Fe]$.

With our cluster sample, we agree with the previous claim by McWilliam et al. (1992) regarding the presence of a strong Al enhancement in NGC 2298. However, our large sample confirms, for the first time, the presence of a clear Mg–Al anti-correlation in NGC 2298, whose proton-burning Mg–Al cycle drives the excess of Al through the reduced surface abundances of ^{24}Mg (see e.g., Ward & Fowler 1980).

We also find that the RGB and AGB stars do not group separately in any of the abundance–abundance planes presented in Fig. 5. Therefore, the observed Mg–Al anti-correlation in NGC 2298 does not depend on the evolutionary status of a star.

6.3. Iron-peak elements (Fe and Ni)

We find a mean metallicity $\langle [Fe/H] \rangle = -1.76 \pm 0.01$ with a dispersion of $\sigma_{[Fe/H]} = 0.048 \pm 0.009$ dex. Reported errors are errors on the mean. We also find an iron star-to-star spread of 0.14 dex, compatible with the measurement errors, so we have no evidence for an intrinsic Fe abundance spread in NGC 2298. Our measured mean metallicity for this GC exhibits a deviation greater than the uncertainties in comparison to some previous works that employ a variety of methods reporting a wide range (~ 0.25 dex) of metallicity from $[Fe/H] = -1.96$ to -1.71 , but it is in reasonable agreement with a few of them. For instance, Frogel et al. (1983) transformed optical and NIR colors to Cohen’s metallicity scale (Cohen 1983), and they estimated a mean value of $[Fe/H] = -1.76$, which has been listed as $[Fe/H]_{\text{IR}}$ in Table 5 of Zinn & West (1984); Zinn & West (1984) found a mean metallicity of $[Fe/H] = -1.85$; Zinn (1985) found a $[Fe/H] = -1.81$ on his metallicity scale; McWilliam et al. (1992) found a metallicity of $[Fe/H] = -1.91$; Geisler et al. (1995) estimated a metallicity of $[Fe/H] = -1.82$; Salaris & Cassisi (1996) reported a metallicity of $[Fe/H] = -1.91$; Carretta & Gratton (1997) reported a metallicity of $[Fe/H] = -1.71$; while Kraft & Ivans (2003) listed a range of metallicity $[Fe/H]$ between -1.93 and -1.83 ;

Pritzl et al. (2005) reported a metallicity of $[Fe/H] = -1.90$; Carretta et al. (2009a) provided a metallicity of $[Fe/H] = -1.96$; Carrera et al. (2013) listed a $[Fe/H] = -1.74$; while more recently Roediger et al. (2014) and Yong et al. (2014) have provided a metallicity estimation of $[Fe/H] = -1.95$ and $[Fe/H] = -1.96$, respectively.

As far as other iron-peak elements are concerned, Ni is slightly overabundant relative to Solar ($+0.12$), with a star-to-star spread of 0.27 dex that is higher than the measurement uncertainties of $[Ni/Fe]$ abundance ratios in NGC 2298, which strikingly appear to be weakly correlated with $[Ca/Fe]$, as can be appreciated in Fig. 5. However, the observed star-to-star spread in the $[Ca/Fe]$ abundance ratios is not statistically significant according to our error analysis, as has been observed in other GCs (Carretta & Bragaglia 2021). Our sample is tightly concentrated around the mean $[Ca/Fe]$ of NGC 2298. Therefore, with the determinations of $[Ni/Fe]$ and $[Ca/Fe]$ for a limited sample of six cluster stars, we cannot draw firm conclusions about the apparent correlation between these two species. This possibility will have to be considered using larger future samples.

7. Concluding remarks

We have performed a high-resolution spectral analysis for 12 stars in the old GC NGC 2298. This cluster is located in a region of low interstellar reddening, and it has a halo orbit that crosses the Bulge, with an apocentric distance of ~ 16.44 kpc (Massari et al. 2019). We found a mean and median metallicity of $[Fe/H] = -1.76$ and -1.75 , respectively, with a star-to-star spread of 0.14 dex that is compatible with the measurement errors, so we find no evidence for an intrinsic Fe abundance spread in NGC 2298. Our reported metallicity is ~ 0.2 dex more metal-rich than previously thought, but it is in reasonable agreement with estimations provided by Kraft & Ivans (2003) and Carrera et al. (2013).

We confirm the existence of an Al-enriched population in NGC 2298, as was claimed three decades ago. We provide, for the first time, evidence for the standard anti-correlation between Mg and Al in our data. This result indicates the prevalence of the MPs phenomenon at the low metallicity of NGC 2298. It is also important to note that RGB and AGB stars present in NGC 2298 do not appear to follow different paths or group separately in any of the abundance planes examined in this work; therefore, we conclude that the observed Mg–Al anti-correlation does not depend on the evolutionary status of a star in NGC 2298. We also detect an apparent Mg–Si anti-correlation and an Al–Si correlation, which are likely signatures of ^{28}Si leakage from the Mg–Al chain, which is a feature common to other GCs (Masseron et al. 2019; Mészáros et al. 2020) at a similar metallicity as NGC 2298.

Acknowledgements. We thank the useful discussions and comments from Baitian Tang, Christian Nitschelm, and an anonymous referee to improve the manuscript. J.G.F.-T. gratefully acknowledges the grant support provided by Proyecto Fondecyt Iniciación No. 11220340, from ANID Concurso de Fomento a la Vinculación Internacional para Instituciones de Investigación Regionales (Modalidad corta duración) Proyecto No. FOVI210020, and also from the grant support from the Joint Committee ESO-Government of Chile 2021 (ORP 023/2021). S.V. gratefully acknowledges the support provided by Fondecyt regular n. 1220264, and by the ANID BASAL projects ACE210002 and FB210003. T.C.B. acknowledges partial support for this work from grant PHY 14-30152: Physics Frontier Center/JINA Center for the Evolution of the Elements (JINACEE), awarded by the US National Science Foundation. B.B. acknowledges grants from FAPESP, CNPq and CAPES – Financial code 001. D.M. gratefully acknowledges support by the ANID BASAL projects ACE210002 and FB210003, and Fondecyt Project No. 1220724. E.R.G. acknowledges support

from ANID PhD scholarship No. 21210330. D.G. gratefully acknowledges support from the ANID BASAL project ACE210002. D.G. also acknowledges financial support from the Dirección de Investigación y Desarrollo de la Universidad de La Serena through the Programa de Incentivo a la Investigación de Académicos (PIA-DIDULS). Funding for the Sloan Digital Sky Survey IV has been provided by the Alfred P. Sloan Foundation, the U.S. Department of Energy Office of Science, and the Participating Institutions. SDSS-IV acknowledges support and resources from the Center for High-Performance Computing at the University of Utah. The SDSS web site is www.sdss.org. SDSS-IV is managed by the Astrophysical Research Consortium for the Participating Institutions of the SDSS Collaboration including the Brazilian Participation Group, the Carnegie Institution for Science, Carnegie Mellon University, the Chilean Participation Group, the French Participation Group, Harvard-Smithsonian Center for Astrophysics, Instituto de Astrofísica de Canarias, The Johns Hopkins University, Kavli Institute for the Physics and Mathematics of the Universe (IPMU)/University of Tokyo, Lawrence Berkeley National Laboratory, Leibniz Institut für Astrophysik Potsdam (AIP), Max-Planck-Institut für Astronomie (MPIA Heidelberg), Max-Planck-Institut für Astrophysik (MPA Garching), Max-Planck-Institut für Extraterrestrische Physik (MPE), National Astronomical Observatory of China, New Mexico State University, New York University, University of Notre Dame, Observatório Nacional/MCTI, The Ohio State University, Pennsylvania State University, Shanghai Astronomical Observatory, United Kingdom Participation Group, Universidad Nacional Autónoma de México, University of Arizona, University of Colorado Boulder, University of Oxford, University of Portsmouth, University of Utah, University of Virginia, University of Washington, University of Wisconsin, Vanderbilt University, and Yale University. This work has made use of data from the European Space Agency (ESA) mission *Gaia* (<http://www.cosmos.esa.int/gaia>), processed by the *Gaia* Data Processing and Analysis Consortium (DPAC, <http://www.cosmos.esa.int/web/gaia/dpac/consortium>). Funding for the DPAC has been provided by national institutions, in particular the institutions participating in the *Gaia* Multilateral Agreement.

References

- Abdurro'uf, Accetta, K., Aerts, C., et al. 2022, *ApJS*, **259**, 35
- Asplund, M., Grevesse, N., & Sauval, A. J. 2005, in *Cosmic Abundances as Records of Stellar Evolution and Nucleosynthesis*, eds. I. Barnes, G. Thomas, & F. N. Bash, *ASP Conf. Ser.*, **336**, 25
- Balbinot, E., Santiago, B. X., da Costa, L. N., Makler, M., & Maia, M. A. G. 2011, *MNRAS*, **416**, 393
- Bastian, N., & Lardo, C. 2018, *ARA&A*, **56**, 83
- Baumgardt, H., & Vasiliev, E. 2021, *MNRAS*, **505**, 5957
- Beaton, R. L., Oelkers, R. J., Hayes, C. R., et al. 2021, *AJ*, **162**, 302
- Belokurov, V., Erkal, D., Evans, N. W., Koposov, S. E., & Deason, A. J. 2018, *MNRAS*, **478**, 611
- Blanton, M. R., Bershad, M. A., Abolfathi, B., et al. 2017, *AJ*, **154**, 28
- Bowen, I. S., & Vaughan, A. H., Jr. 1973, *Appl. Opt.*, **12**, 1430
- Bressan, A., Marigo, P., Girardi, L., et al. 2012, *MNRAS*, **427**, 127
- Carballo-Bello, J. A., Martínez-Delgado, D., Navarrete, C., et al. 2018, *MNRAS*, **474**, 683
- Carrera, R., Pancino, E., Gallart, C., & del Pino, A. 2013, *MNRAS*, **434**, 1681
- Carretta, E., & Gratton, R. G. 1997, *A&AS*, **121**, 95
- Carretta, E., & Bragaglia, A. 2021, *A&A*, **646**, A9
- Carretta, E., Bragaglia, A., Gratton, R., D'Orazi, V., & Lucatello, S. 2009a, *A&A*, **508**, 695
- Carretta, E., Bragaglia, A., Gratton, R., & Lucatello, S. 2009b, *A&A*, **505**, 139
- Cohen, J. G. 1983, *ApJ*, **270**, 654
- Crane, J. D., Majewski, S. R., Rocha-Pinto, H. J., et al. 2003, *ApJ*, **594**, L119
- Cunha, K., Smith, V. V., Hesselquist, S., et al. 2017, *ApJ*, **844**, 145
- Fernández-Trincado, J. G., Zamora, O., Souto, D., et al. 2019, *A&A*, **627**, A178
- Fernández-Trincado, J. G., Beers, T. C., Minniti, D., et al. 2020, *A&A*, **643**, L4
- Fernández-Trincado, J. G., Beers, T. C., Barbuy, B., et al. 2021a, *ApJ*, **918**, L9
- Fernández-Trincado, J. G., Beers, T. C., Minniti, D., et al. 2021b, *A&A*, **647**, A64
- Fernández-Trincado, J. G., Villanova, S., Geisler, D., et al. 2022, *A&A*, **658**, A116
- Forbes, D. A., & Bridges, T. 2010, *MNRAS*, **404**, 1203
- Frogel, J. A., Cohen, J. G., & Persson, S. E. 1983, *ApJ*, **275**, 773
- García Pérez, A. E., Allende Prieto, C., Holtzman, J. A., et al. 2016, *AJ*, **151**, 144
- Geisler, D., Piatti, A. E., Claria, J. J., & Minniti, D. 1995, *AJ*, **109**, 605
- Geisler, D., Villanova, S., O'Connell, J. E., et al. 2021, *A&A*, **652**, A157
- Gunn, J. E., Siegmund, W. A., Mannery, E. J., et al. 2006, *AJ*, **131**, 2332
- Gustafsson, B., Edvardsson, B., Eriksson, K., et al. 2008, *A&A*, **486**, 951
- Hasselquist, S., Shetrone, M., Cunha, K., et al. 2016, *ApJ*, **833**, 81
- Helmi, A., Babusiaux, C., Koppelman, H. H., et al. 2018, *Nature*, **563**, 85
- Hesser, J. E., & Shawl, S. J. 1985, *PASP*, **97**, 465
- Holtzman, J. A., Hesselquist, S., Shetrone, M., et al. 2018, *AJ*, **156**, 125
- Ibata, R., Malhan, K., Martin, N., et al. 2021, *ApJ*, **914**, 123
- Jönsson, H., Allende Prieto, C., Holtzman, J. A., et al. 2018, *AJ*, **156**, 126
- Jönsson, H., Holtzman, J. A., Allende Prieto, C., et al. 2020, *AJ*, **160**, 120
- Kraft, R. P., & Ivans, I. I. 2003, *PASP*, **115**, 143
- Leon, S., Meylan, G., & Combes, F. 2000, *A&A*, **359**, 907
- Majewski, S. R., Schiavon, R. P., Frinchaboy, P. M., et al. 2017, *AJ*, **154**, 94
- Malhan, K., Ibata, R. A., Sharma, S., et al. 2022, *ApJ*, **926**, 107
- Marino, A. F., Milone, A. P., Renzini, A., et al. 2021, *ApJ*, **923**, 22
- Martin, N. F., Ibata, R. A., Bellazzini, M., et al. 2004, *MNRAS*, **348**, 12
- Massari, D., Koppelman, H. H., & Helmi, A. 2019, *A&A*, **630**, L4
- Masseron, T., García-Hernández, D. A., Mészáros, S., et al. 2019, *A&A*, **622**, A191
- Masseron, T., Merle, T., & Hawkins, K. 2016, *Astrophysics Source Code Library* [record ascl:1605.004]
- McWilliam, A., Geisler, D., & Rich, R. M. 1992, *PASP*, **104**, 1193
- Mészáros, S., Martell, S. L., Shetrone, M., et al. 2015, *AJ*, **149**, 153
- Mészáros, S., Masseron, T., García-Hernández, D. A., et al. 2020, *MNRAS*, **492**, 1641
- Mészáros, S., Masseron, T., Fernández-Trincado, J. G., et al. 2021, *MNRAS*, **505**, 1645
- Milone, A. P., Piotto, G., Renzini, A., et al. 2017, *MNRAS*, **464**, 3636
- Monty, S., Puzia, T. H., Miller, B. W., et al. 2018, *ApJ*, **865**, 160
- Nidever, D. L., Holtzman, J. A., Allende Prieto, C., et al. 2015, *AJ*, **150**, 173
- Pancino, E., Romano, D., Tang, B., et al. 2017, *A&A*, **601**, A112
- Piatti, A. E., & Carballo-Bello, J. A. 2020, *A&A*, **637**, L2
- Piotto, G., Milone, A. P., Bedin, L. R., et al. 2015, *AJ*, **149**, 91
- Pritzl, B. J., Venn, K. A., & Irwin, M. 2005, *AJ*, **130**, 2140
- Rani, S., Pandey, G., Subramaniam, A., et al. 2021, *ApJ*, **923**, 162
- Roediger, J. C., Courteau, S., Graves, G., & Schiavon, R. P. 2014, *ApJS*, **210**, 10
- Salaris, M., & Cassisi, S. 1996, *A&A*, **305**, 858
- Santana, F. A., Beaton, R. L., Covey, K. R., et al. 2021, *AJ*, **162**, 303
- Schiavon, R. P., Johnson, J. A., Frinchaboy, P. M., et al. 2017, *MNRAS*, **466**, 1010
- Shetrone, M., Bizyaev, D., Lawler, J. E., et al. 2015, *ApJS*, **221**, 24
- Smith, V. V., Bizyaev, D., Cunha, K., et al. 2021, *AJ*, **161**, 254
- Sollima, A. 2020, *MNRAS*, **495**, 2222
- Tsujimoto, T., & Bekki, K. 2012, *ApJ*, **751**, L35
- Vasiliev, E., & Baumgardt, H. 2021, *MNRAS*, **505**, 5978
- Ward, R. A., & Fowler, W. A. 1980, *ApJ*, **238**, 266
- Wilson, J. C., Hearty, F. R., Skrutskie, M. F., et al. 2019, *PASP*, **131**
- Yong, D., Grundahl, F., Nissen, P. E., Jensen, H. R., & Lambert, D. L. 2005, *A&A*, **438**, 875
- Yong, D., Roederer, I. U., Grundahl, F., et al. 2014, *MNRAS*, **441**, 3396
- Zamora, O., García-Hernández, D. A., Allende Prieto, C., et al. 2015, *AJ*, **149**, 181
- Zasowski, G., Cohen, R. E., Chojnowski, S. D., et al. 2017, *AJ*, **154**, 198
- Zhang, S., Mackey, D., & Da Costa, G. S. 2022, *MNRAS*, **513**, 3136
- Zinn, R. 1985, *ApJ*, **293**, 424
- Zinn, R., & West, M. J. 1984, *ApJS*, **55**, 45

Appendix A: Basic parameters of NGC 2298 stars

The basic parameters for the 12 NGC 2298 members examined in this work are listed in Table A.1.

Table A.1. *Gaia* EDR3 photometric and astrometric, APOGEE-2S radial velocity, photometric atmospheric (T_{eff} , $\log(g)$ and ξ_t) properties, and BACCHUS elemental abundances for 12 stars in the innermost regions of NGC 2298. The cluster median, mean, and standard deviation from BACCHUS and ASPCAP, as well as the BACCHUS spread are listed in the last rows.

APOGEE_ID	Class	G	B _p	R _p	$\mu_\alpha \cos(\delta) \pm \Delta$ mas yr ⁻¹	$\mu_\delta \pm \Delta$ mas yr ⁻¹	RV km s ⁻¹	S/N pixel ⁻¹	T _{eff} K	log(<i>g</i>) [cgs]	ξ_t km s ⁻¹	[Mg/Fe]	[Al/Fe]	[Si/Fe]	[Ca/Fe]	[Fe/H]	[Ni/Fe]
2M06485459–3559151	RGB	13.89	14.61	13.06	3.18±0.01	−2.21±0.01	147.35	156	4685	1.34	1.95	+0.09 (0.09)	+0.65 (0.07)	+0.32 (0.07)	...	−1.74 (0.11)	+0.03 (0.09)
2M06485872–3600006	RGB	13.75	14.43	12.92	3.28±0.01	−2.18±0.01	147.61	174	4652	1.27	1.98	+0.16 (0.08)	−0.27 (0.07)	+0.26 (0.15)	...	−1.74 (0.12)	+0.05 (0.10)
2M06485886–3558262	RGB	13.87	14.57	13.06	3.35±0.01	−2.14±0.01	146.71	166	4683	1.33	1.96	+0.15 (0.15)	−0.19 (0.11)	+0.29 (0.11)	+0.32 (0.09)	−1.71 (0.11)	+0.06 (0.09)
2M06485916–3600503	RGB	13.80	14.50	12.97	3.33±0.01	−2.25±0.01	142.10	169	4663	1.29	1.97	+0.18 (0.12)	−0.20 (0.15)	+0.25 (0.07)	+0.46 (0.07)	−1.72 (0.10)	+0.25 (0.10)
2M06490301–3559100	RGB	13.80	14.50	12.98	3.34±0.01	−2.13±0.01	145.75	157	4665	1.30	1.97	+0.11 (0.12)	+0.06 (0.11)	+0.24 (0.07)	+0.32 (0.06)	−1.71 (0.09)	...
2M06490382–3600299	RGB	14.97	15.56	14.20	3.40±0.02	−2.23±0.02	152.96	109	4943	1.89	1.75	+0.24 (0.05)	−0.42 (0.03)	+0.25 (0.11)	...	−1.75 (0.16)	...
2M06490734–3558013	RGB	13.63	14.35	12.81	3.30±0.01	−2.13±0.01	144.48	190	4620	1.21	2.00	+0.22 (0.11)	−0.23 (0.14)	+0.27 (0.12)	+0.33 (0.08)	−1.72 (0.09)	+0.07 (0.08)
2M06491677–3557505	RGB	14.07	14.72	13.28	3.31±0.01	−2.20±0.01	148.22	139	4733	1.44	1.92	+0.01 (0.12)	+0.87 (0.09)	+0.25 (0.15)	+0.37 (0.05)	−1.75 (0.11)	+0.07 (0.08)
2M06485140–3600380	AGB	13.93	14.55	13.17	3.27±0.01	−2.06±0.01	147.95	138	4795	1.39	2.03	−0.07 (0.08)	+0.87 (0.09)	+0.42 (0.12)	+0.45 (0.05)	−1.87 (0.17)	+0.36 (0.03)
2M06485619–3602261	AGB	14.78	15.32	14.06	3.37±0.01	−2.19±0.01	150.23	112	5059	1.84	1.90	+0.18 (0.05)	−0.40 (0.06)	+0.21 (0.13)	...	−1.83 (0.18)	...
2M06485888–3601165	AGB	13.09	13.85	12.22	3.38±0.01	−2.18±0.01	144.04	254	4517	0.91	2.17	+0.19 (0.11)	−0.18 (0.13)	+0.28 (0.07)	+0.39 (0.05)	−1.78 (0.10)	+0.08 (0.09)
2M06485948–3559426	AGB	14.40	14.93	13.58	3.43±0.01	−2.24±0.01	141.92	116	4935	1.63	1.95	−0.06 (0.03)	+0.86 (0.07)	+0.35 (0.18)	...	−1.80 (0.16)	+0.11 (0.11)
BACCHUS																	
Cluster median	+0.16	−0.19	+0.27	+0.37	−1.75	+0.07
Cluster mean	+0.12	+0.12	+0.29	+0.38	−1.76	+0.12
Std	0.10	0.51	0.05	0.05	0.05	0.10
Spread†	0.30	1.29	0.15	0.13	0.14	0.27

†Spread is defined as the 95th percentile - 5th percentile. The listed uncertainty inside parentheses for each chemical species is as follows: $\sigma_{\text{total}} = \sqrt{\sigma_{T_{\text{eff}}}^2 + \sigma_{\log g}^2 + \sigma_{\xi_t}^2 + \sigma_{\text{mean}}^2}$, where σ_{mean}^2 was calculated using the standard deviation from the different abundances of the different lines for each element, while $\sigma_{T_{\text{eff}}}^2$, $\sigma_{\log g}^2$, and $\sigma_{\xi_t}^2$ were derived for each chemical species while varying T_{eff} by ± 100 K, $\log g$ by ± 0.3 dex, and ξ_t by ± 0.05 km s⁻¹.